

BAR-HALO FRICTION IN GALAXIES I: SCALING LAWS

J. A. SELLWOOD

Rutgers University, Department of Physics & Astronomy,
136 Frelinghuysen Road, Piscataway, NJ 08854-8019
sellwood@physics.rutgers.edu

To appear in ApJ

ABSTRACT

It has been known for some time that rotating bars in galaxies slow due to dynamical friction against the halo. However, recent attempts to use this process to place constraints on the dark matter density in galaxies and possibly also to drive dark matter out of the center have been challenged. This paper uses simplified numerical experiments to clarify several aspects of the friction mechanism. I explicitly demonstrate the Chandrasekhar scaling of the friction force with bar mass, halo density, and halo velocity dispersion. I present direct evidence that exchanges between the bar and halo orbits at major resonances are responsible for friction and study both individual orbits and the net changes at these resonances. I also show that friction alters the phase space density of particles in the vicinity of a major resonance, which is the reason the magnitude of the friction force depends on the prior evolution. I demonstrate that bar slow down can be captured correctly in simulations having modest spatial resolution and practicable numbers of particles. Subsequent papers in this series delineate the dark matter density that can be tolerated in halos of different density profiles.

Subject headings: galaxies: formation — galaxies: kinematics and dynamics — galaxies: halos — dark matter

1. INTRODUCTION

Friction between a rotating bar and a massive halo was first reported many years ago (Sellwood 1980) and has subsequently been worked on sporadically (Tremaine & Weinberg 1984; Weinberg 1985; Little & Carlberg 1991; Hernquist & Weinberg 1992; Athanassoula 1996). It has, however, received a lot of attention in recent years as a potential probe of, and structuring mechanism for, dark matter halos. Debattista & Sellwood (1998, 2000) argued that the fact that bars appear not to have been slowed places an upper bound on the density of the dark matter halo in barred disk galaxies. Weinberg & Katz (2002) argue that the transfer of angular momentum from the bar to the halo could reduce the central density of the dark matter halo by a substantial factor.

Both of these claims have subsequently been disputed; Valenzuela & Klypin (2003) claim a counter-example of a bar that does not experience much friction in a “cosmologically-motivated” halo and Holley-Bockelmann & Weinberg (2005) find that cleverly-constructed uniform-density halos can also avoid friction. The argument by Athanassoula (2003) that weak bars experience little friction is clearly correct, but irrelevant for strong bars. Only modest reductions in halo density have been achieved so far (Holley-Bockelmann, Weinberg & Katz 2003) and Sellwood (2003) found that contraction of the disk mass distribution as it lost angular momentum to the halo dragged halo mass in with it, causing the density to rise, rather than to decrease.

Valenzuela & Klypin (2003) and Holley-Bockelmann, *et al.* blame discrepant conclusions on inadequacies respectively of the codes and of the number of particles employed, but it is also likely that a good part of the differences reported by these authors arise because the physical models differ. There have been a few tests with different codes from the same initial conditions and the results compare quite well (*e.g.* O’Neill & Dubinski 2003; Sellwood 2003);

other comparisons are reported here and in Papers II & III (Sellwood & Debattista 2005a,b).

The present paper attempts to clarify the physics of dynamical friction between a bar and a halo and to show that it can be correctly reproduced in simulations of a size that is readily accessible with current computational resources. The counter-example reported by Valenzuela & Klypin (2003) is addressed in Sellwood & Debattista (2005c) and Paper II. The constraint on halo density that can be deduced from the existence of strong, fast bars and criticisms by Athanassoula (2003) are addressed in Paper III.

2. THEORETICAL BACKGROUND

Dynamical friction (Chandrasekhar 1943) is the retarding force experienced by a massive perturber moving through a background of low-mass particles. It arises, even in a perfectly collisionless system, from the vector sum of the impulses the perturber receives from the particles as they are deflected by its gravitational field. Equivalently, friction can be viewed as the gravitational attraction on the perturber of the density excess, or wake, that develops behind it as it moves, as was nicely illustrated by Mulder (1983).

Chandrasekhar’s formula (eq. 7-17 of Binney & Tremaine 1987; hereafter BT) for the acceleration a_M of a perturber of mass M moving at speed v_M through a uniform background, density ρ , of non-interacting particles having an isotropic velocity distribution with a 1-D rms velocity spread σ , may be written as

$$a_M(v_M) = 4\pi \ln \Lambda G^2 \frac{M\rho}{\sigma^2} V\left(\frac{v_M}{\sigma}\right). \quad (1)$$

Here, Λ ($= b_{\max}/b_{\min}$) is the argument of the usual Coulomb logarithm, and the dimensionless function V is drawn in Figure 1 for a Gaussian distribution of velocities; other velocity distributions would yield a different

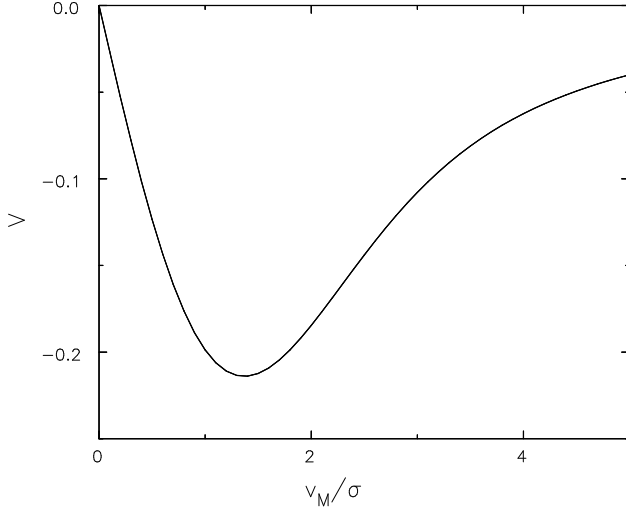


FIG. 1.— The dimensionless acceleration function V defined in equation (1) for the case of a Gaussian distribution of velocities among the background particles.

functional form.

The simplifying assumptions in its derivation strictly invalidate application of equation (1) to the physically more interesting problem of friction in a non-uniform medium in which the background particles are confined by a potential well and interact with the perturber repeatedly. Repeated encounters between the perturber and the background particles require a more sophisticated treatment.

2.1. Orbits and resonances

The motion of a particle pursuing a regular orbit in a smooth ellipsoidal potential is triply periodic, and is most conveniently described by action-angle variables (see BT).¹ The three angular momentum-like actions, \mathbf{J} , describe the amount of “round and round”, “in and out” and “up and down” motion associated with the orbit, while the angles, \mathbf{w} , specify the phases of these three separate oscillations that underlie the motion. One of the many advantages of these variables is that the angles are defined such that they increase at a uniform rate $\dot{\mathbf{w}} \equiv \Omega(\mathbf{J})$ for each orbit.

In this paper, as in most other discussions, we will be concerned with mild perturbations to a spherical potential, where the unperturbed motion of any particle is confined to a plane. In this case, there are just two non-zero actions: the azimuthal action $J_\phi \equiv L$, the total specific angular momentum, and the radial action, J_r . The motion is then simply doubly periodic at angular rates Ω_ϕ and Ω_r .

The angular frequency, Ω_ϕ , of a particle’s mean motion about the center is, in general, incommensurable with its angular frequency of radial motion, Ω_r . However, all orbits can appear to close when viewed from many different rotating frames. An observer rotating at the rate

$$\Omega' = \Omega_\phi + k\Omega_r/m, \quad (2)$$

would see the orbit close after m radial oscillations and k

¹Irregular orbits that do not preserve three integrals of motion may be important in real galaxies, but most discussion of dynamical friction has focused on simple (usually spherical) potentials in which all unperturbed orbits are regular.

turns about the center; Kalnajs (1977) draws an orbit in several of the most important frames.

The angular momentum vectors of orbits in a spherical system are distributed over all angles. We define some direction as the z -axis and use θ for the angle between that axis and the plane of each unperturbed orbit, with θ having the same sign as the z -component of the angular momentum $L_z = L \sin \theta$. The frequencies of the motion projected into the equatorial plane, $\theta = \pi/2$, are independent of θ , save only that the sign of Ω_ϕ is that of L_z .

We are interested in an ellipsoidal bar-like perturbation that rotates about its minor axis, which we take to be the z -axis. If the bar rotates at an angular speed Ω_b , there are many possible resonances between the orbits of the particles and the perturbing potential. Resonances occur where $m\Omega_b = n\Omega_\phi + k\Omega_r$, where $(m, k, n) \equiv \mathbf{m}$ are three integers; m is even for a bar, $n = 0, \pm m$, and $-1 \leq k \leq \infty$ (Tremaine & Weinberg 1984). Three of the most important resonances are familiar from disk dynamics: the corotation resonance (CR) where $n = m$ and $k = 0$, the inner Lindblad resonance (ILR) where $n = m = 2$ and $k = -1$, and the outer Lindblad resonance (OLR) where $n = m = 2$ and $k = 1$. Negative values of n lead to resonances with retrograde particles, which seem to be of little dynamical importance. Weinberg & Katz (2005; hereafter WK05) stress the importance a fourth: the direct radial resonance (DRR) for which $n = 0$ and $k = 1$. This last resonance is absent for orbits in the bar plane and is most important for near polar orbits.

2.2. Friction in spheroidal systems

Tremaine & Weinberg (1984, hereafter TW84) developed the basic theory of dynamical friction by a generic perturber in spherical systems. Following the precepts of Lynden-Bell & Kalnajs (1972), they derived an expression for the “LBK torque” in a spherical system, which they showed arises purely at resonances. Weinberg (1985) gave a specific evaluation of the LBK torque for the case of a bar. The role of resonances has been re-emphasized in recent work (Weinberg & Katz 2002; Athanassoula 2003; Holley-Bockelmann, *et al.* 2003; WK05).

As for the classical Chandrasekhar problem, friction can be viewed in two equivalent ways: it can be seen either as arising from the gravitational coupling between the bar and a misaligned density response in the halo, or it can be interpreted as the net effect of exchanges at resonances between the particles and the perturber. The misalignment can be understood in terms of interactions at resonances, where halo particles gain or lose angular momentum.

The daunting expression for the LBK torque derived by TW84 (their eq. 65) does not appear to resemble eq. (1) above. However, TW84 also reformulate the original Chandrasekhar problem in a manner that highlights the similarities with the LBK torque in a spherical system, but which contains no resonant terms because the system is infinite. A naïve guess, therefore, is that the LBK torque causes the angular acceleration of the perturber to scale as

$$\dot{\Omega}_p \propto \frac{M_p \rho_s}{\sigma_s^2} \Theta \left(\frac{\Omega_p a}{\sigma_s} \right), \quad (3)$$

where M_p is the mass of the perturber, ρ_s and σ_s are the characteristic density and velocity dispersion of the spher-

ical system, and the dimensionless function Θ contains all the complicated dependence on the details of the distribution function, potential well, resonances, bar shape, *etc.* A characteristic length scale a is included in order to make the argument of Θ dimensionless. The functions $\Theta(x)$ and $V(x)$ share the general properties that they are negative, at least for isotropic distribution functions (TW84), they must $\rightarrow 0$ as $x \rightarrow \infty$, and that they can reasonably be expected to be $\propto x$ as $x \rightarrow 0$.

Weinberg (2004) points out that the LBK torque formula derived by TW84 is not the full story, because their expression is evaluated for a perturbation of fixed amplitude and pattern speed. Weinberg finds that the torque depends strongly on the previous time-dependence of the perturbation, which he needed to take into account in order to reconcile his perturbation theory with results from his simulations. This improvement to the theory is a major step forward, as we show here.

2.3. Motivation

The numerical experiments of Lin & Tremaine (1983) showed that a satellite orbiting a spherical system composed of much lighter particles confined in a potential well experiences a frictional force that scales very much as predicted by eq. (1), or eq. (3), despite the complications caused by resonances. This, and other evidence, led BT to conclude that “Chandrasekhar’s formula often provides a remarkably accurate description of the drag experienced by a body orbiting in a stellar system”.

We might hope that the Chandrasekhar scaling would also hold for bars, but there is no detailed check in the literature. Weinberg (1985) reports a few crude simulations of the Lin & Tremaine type in support of his theoretical calculations and he remarks (Weinberg 2004) that he has recently made more such tests.

In §§4&5 I present a much more extensive study using the Lin & Tremaine technique for this slightly different physical problem, and show that the expected scaling of eq. (3) holds quite well. §6 reports a more detailed study of resonant exchanges both of individual orbits and of the ensemble of particles. §7 confirms Weinberg’s (2004) finding that the time dependence of the perturbation is of major importance, and offers an explanation. I present convergence tests without self-gravity in §8 and I include the effects of self-gravity between the halo particles in §9 in order to determine empirically the numbers of particles needed to reproduce the correct frictional force in fully self-consistent simulations.

3. MODELS AND METHOD

3.1. Halo models

I create an N -body realization of a spherical mass distribution, which for brevity I describe as a halo, although it could be any spherical system of collisionless particles. In §4, the particles move in the smooth analytic gravitational potential of the adopted halo and I neglect any interaction forces between the particles. Since I draw the particles from a distribution function (DF) that generates the adopted halo density, the particle distribution is in equilibrium and does not evolve in the absence of an external perturbation. The isotropic halos start with no net angular momentum.

I use three quite different halo models. The first is a Hernquist (1990) model, which has the density profile

$$\rho_H(r) = \frac{M_H r_H}{2\pi r(r_H + r)^3}, \quad (4)$$

with total mass M_H . The density profile declines as r^{-1} for $r \ll r_H$ and as r^{-4} for $r \gg r_H$. It should be noted that this model differs only slightly from the NFW profile (see Appendix), which appeared to be a reasonable fit to early simulations (Navarro, Frenk & White 1997) of the collapse of dark matter halos. Hernquist gives the expression for the isotropic DF that generates the halo of eq. (4). I do not employ the infinite model, but remove from the DF any particle with sufficient energy to reach $r > 20r_H$, so that the active mass in particles is $\sim 0.86M_H$ while they move in the analytic potential of the untruncated halo. The active density profile is very little affected for $r < 15r_H$, while the bars I employ are typically much smaller, with semi-major axes $\sim r_H$.

I have also employed the well-known Plummer sphere

$$\rho_P(r) = \frac{3M_H}{4\pi r_P^3} \left(1 + \frac{r^2}{r_P^2} \right)^{-5/2}, \quad (5)$$

which has a uniform density core. The isotropic DF that generates this density profile is a polytrope of index $n = 5$ (BT, equation 4-104). Again I eliminate any particle with sufficient energy to reach $r > 20r_P$, which is less than 1% of the mass.

As a third halo model, I have adopted the singular isothermal sphere (SIS), which formally has the scale-free density profile

$$\rho_I(r) = \frac{V_0^2}{4\pi G r^2}. \quad (6)$$

An isotropic DF that generates this density has a 1-D velocity dispersion $\sigma = V_0/\sqrt{2}$. The particles move in the exact logarithmic potential of the untruncated sphere, but I generate active particles from this DF with a limited range of energies. The upper bound is set so that no particle has enough energy to pass an outer radius r_{\max} , while the lower bound eliminates any particle that would be bound inside some small radius r_{\min} . I choose $r_{\max} = 20a$ and $r_{\min} = 0.01a$, where a is my adopted bar semi-major axis. For this model only, I set the mass of each halo particle proportional to $L^{1/2}$, where L is its total angular momentum, in order to obtain a disproportionately higher density of particles in the inner parts of the halo.

3.2. Bar

The bar model is a homogeneous ellipsoid, which has the density distribution

$$\rho_b = \begin{cases} \frac{3M_b}{4\pi abc} & \mu^2 \leq 1 \\ 0 & \mu^2 > 1 \end{cases} \quad (7)$$

where M_b is the mass of the ellipsoid, a , b & c are its semi-axes, with $a \geq b \geq c$, and

$$\mu^2 = \frac{x^2}{a^2} + \frac{y^2}{b^2} + \frac{z^2}{c^2}. \quad (8)$$

I do not use the full field of this bar but employ only non-axisymmetric parts of the field, excluding the monopole term in order not to disturb the radial profile of the halo as I introduce the bar. This approach is similar to that first adopted by Hernquist & Weinberg (1992), who employed only an approximation to the quadrupole term of the bar field. Here, I determine the precise field of the bar using a multipole expansion (*e.g.* BT, §2.4), but use only the non-axisymmetric quadrupole ($l = 2, m = 2$) term, and in some cases higher terms, to accelerate the halo particles. (The odd- l and odd- m terms all vanish because the bar is respectively symmetric about the mid-plane and has 2-fold rotational symmetry, while the $(l, 0)$ terms do not rotate. Because the bar lies in the equatorial plane, terms with $l = m$ will be much larger than those with $l > m > 0$.) The internal and external contributions to the bar field over the radial range of the bar are tabulated only once and stored; it is straightforward to rotate the tabulated values through any desired angle at each step.

The bar rotates at angular frequency Ω_b about its shortest axis, and I introduce the bar smoothly by increasing M_b as a cubic function of time from zero at $t = 0$ to its final value at $t = t_g$. I consider the model bar to be rigid, and to spin down due to loss of angular momentum according to its moment of inertia about the shortest axis, which is

$$I = \frac{M_b}{5}(a^2 + b^2). \quad (9)$$

A rigid bar is essential for this study, even though it is unrealistic in many ways. I must make arbitrary choices for the bar mass, length, axis ratio, density profile, and initial pattern speed, rather than have all these parameters set by the dynamics of a disk. In addition, a rigid bar will not have the same moment of inertia as a figure of the same density profile composed of active particles, which has a pattern speed set by the mean precession rate of the bar particle orbits. Furthermore, the density profile of the bar should change as the bar loses angular momentum and the mean radius of the bar particles decreases, and a bar in an active disk may also grow by trapping extra orbits. The present study, however, requires rigid bars with controlled parameters in order to determine how friction depends on the bar properties.

3.3. Numerical procedure

The halo particles move in the combined fields of the halo and of some non-axisymmetric terms of the rotating bar field. The halo field is rigid in the experiments described in §4, but some self-gravity terms are included in §9. I sum the z -component of the net torque on the particles and use the negative of this sum as the torque acting to accelerate the bar at every step, so that the combined angular momentum of the halo and bar is conserved.

My system of units is such that $G = M_h = r_x = 1$, where $r_x = r_H$ for the Hernquist halo and $r_x = r_P$ for the Plummer halo. For the SIS models, on the other hand, I choose $G = V_0 = a = 1$, for which my unit of mass is aV_0^2/G . Unless otherwise stated, the bar axes are $a : b : c = 1 : 0.5 : 0.05$ and $t_g = 10$ in these units.

As particles in these models have a wide range of frequencies, I divide the computation volume into a number of spherical zones (typically 5) in which particles move with different time steps that differ by factors of 2. The

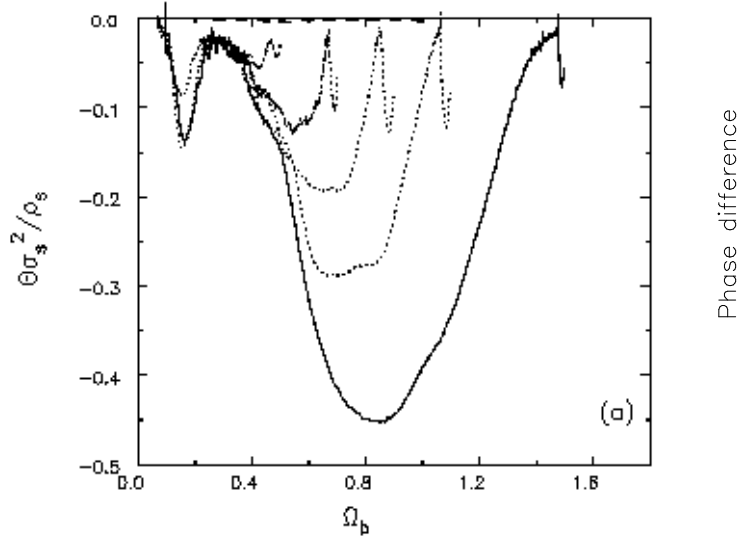


FIG. 2.— (a) The variation of Θ with angular speed of the bar. The solid and dotted curves show the acceleration in response to the quadrupole field of a fat (1:0.5:0.05) bar for different initial Ω_b values. The dashed curve shows the same quantity when the perturbing force is the (4,4) component of the bar field only. (b) The phase lag in radians between the density response in the inner halo and the bar from the run shown by the solid curve in (a). The response is approximately orthogonal to the bar direction when Ω_b is large, and gradually shifts into alignment as the bar slows.

integration step changes when particles cross zone boundaries. I have verified that the results presented here do not depend on this scheme, or on the radii of the zone boundaries, or on the adopted fundamental time step, neither are they affected when the bar quadrupole field is replaced by the smooth function adopted by Hernquist & Weinberg (1992).

4. EXPLORATION OF PARAMETER SPACE

4.1. Scaling with angular speed

The solid curve in Figure 2(a) shows the function Θ for a Hernquist halo and a bar with axis ratios $a : b : c = 1 : 0.5 : 0.1$ and $a = r_H$, when $\Omega_b = 1.5$ initially. (The bar mass $M_b = 0.01M_h$ and the halo is represented by 10M particles.) Over most of the range, the drag force on the bar varies quite smoothly, peaking when $\Omega_b \simeq 0.8$. An initial transient, associated with the turn-on of the bar, is evident, and the curve also has a feature near $\Omega_b \sim 0.2$.

In this case, the initial pattern speed of $\Omega_b = 1.5$ is unrealistically high, and corotation lies well inside the bar, at $r \simeq 0.274a$. The peak deceleration of the bar occurs when corotation lies at the still unrealistically small radius $r \simeq 0.58a$. The pattern speed must drop to $\Omega_b = 0.5$ to place corotation at the end of the bar, by which time the drag force is roughly one third of its peak value.

The dotted curves in Fig. 2(a) show, for identically the same bar and halo, the acceleration in a number of other experiments with lower initial starting speeds. The surprisingly large differences confirm Weinberg's (2004) finding that the friction force depends on the past evolution. The largest differences arise at angular speeds high enough for corotation to lie inside the bar and differences are smaller when $\Omega_b \lesssim 0.5$. I discuss this behavior more fully

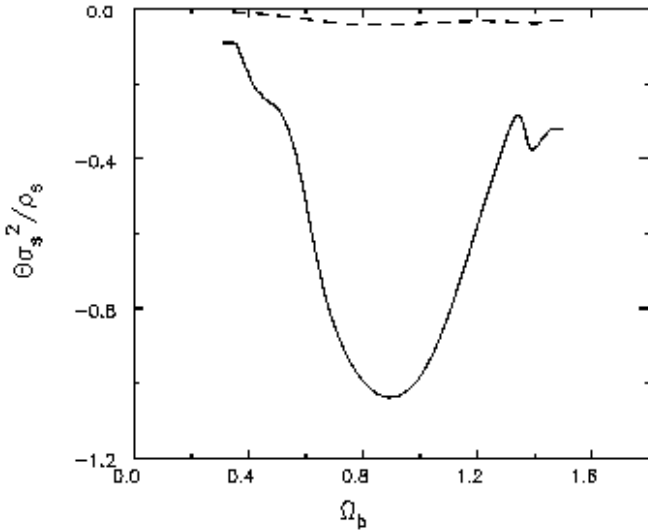


FIG. 3.— As for Fig. 2(a) but for a thinner bar with axis ratios 1:0.2:0.05. Note the different scales between the two figures.

in §7.

Fig. 2(b) shows the lag angle between the principal axes of the bar and of the quadrupole response in the halo as a function of Ω_b for the case when $\Omega_b = 1.5$ initially. I estimate the position angle of the halo density response from the phase of the (2,2) component of a high radial order spherical Bessel function (e.g. Arfken 1985) transform of the particle distribution. It is clear that the response lags the bar by almost a right-angle at high Ω_b , and the lag angle generally decreases as the bar slows, becoming nearly aligned with the bar when its rotation speed is very low. Comparison with Fig. 2(a) confirms, as it must, that the torque is weak when the response is almost orthogonal to, or aligned with, the bar and is greatest as the phase lag passes through intermediate angles. (Since the magnitude of the torque also depends on the amplitude of the response, the maximum need not be when the response is precisely 45° out of phase, although it clearly occurs close to this angle.)

The phase angle of the halo response shown in Fig. 2(b) is not hard to understand. The following argument is specific to spherical potentials, but it generalizes to aspherical cases.

As already noted, any unperturbed orbit will close in a frame that rotates at the rate $\Omega_{\mathbf{m}} = (n\Omega_\phi + k\Omega_r)/m$ ($n \neq 0$), but only those orbits for which $\Omega_{\mathbf{m}} = \Omega_b$ also close in the frame of the rotating perturbation, and are exactly in resonance.

Most orbits are not resonant, however, and $\Omega_{\mathbf{m}} \neq \Omega_b$ for any \mathbf{m} . For these general orbits, the perturbation adds to its otherwise axisymmetric time-averaged density, a forced non-axisymmetric distortion that corotates with the bar. As happens for simple harmonic oscillators, the driven response is in phase, or aligned, with the bar when $\Omega_b < \Omega_{\mathbf{m}}$, and is perpendicular to the bar for higher bar pattern speeds. Thus the forced response of an orbit switches from perpendicular to alignment as the bar slows across its resonant frequency; the change of phase is gradual because the resonance is broadened by the changing pattern speed. Since many orbits are present with a wide range of pre-

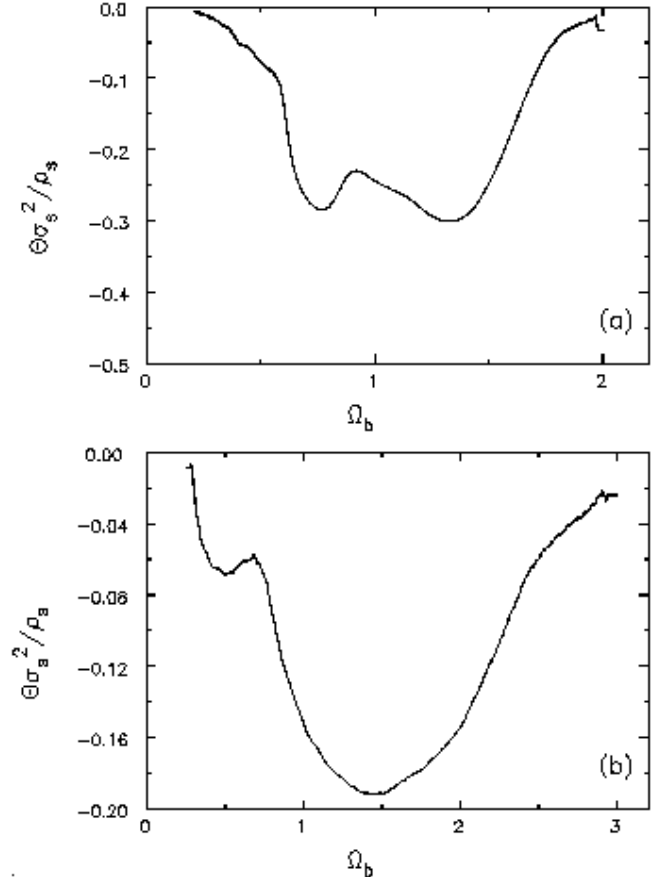


FIG. 4.— As for Fig. 2(a), but (a) for the Plummer halo and (b) for the singular isothermal sphere.

cession rates for each resonance, the net response is the aggregate of many orbits.

4.2. Different strength bar

Fig. 3 shows the much stronger frictional deceleration for a thinner bar with axis ratios 1:0.2:0.05. The quadrupole potential of this bar peaks at about twice the value of the fatter bar used in Fig. 2(a), but at a smaller radius; the two fields could not be matched by scaling, therefore. Nevertheless, the curve has a similar shape.

4.3. Four-fold and higher potential terms

The dashed curves in Figs. 2(a) & 3 show the frictional deceleration for a 20 times more massive bar when only the $l = 4$, $m = 4$ term of the bar field is used to force the halo. Since evolution with a 1% mass bar would be impractically slow, I used a 20% mass bar in both cases, and scaled the curves appropriately. The relative strengths of the quadrupole and higher-order components of the perturbing field depend on the bar shape; the (4,4) component of the potential has a peak amplitude of $\sim 1/6$ that of the quadrupole for the fatter bar, whereas it is a larger fraction ($\sim 1/3$) for the thinner bar. Yet the contribution to friction from the (4,4) term is small even for the sharper bar (Fig. 3); higher order terms are still less important.

Since friction is dominated by only the lowest-order, non-axisymmetric term of the potential, it is possible for even low-spatial resolution codes, such as that used by

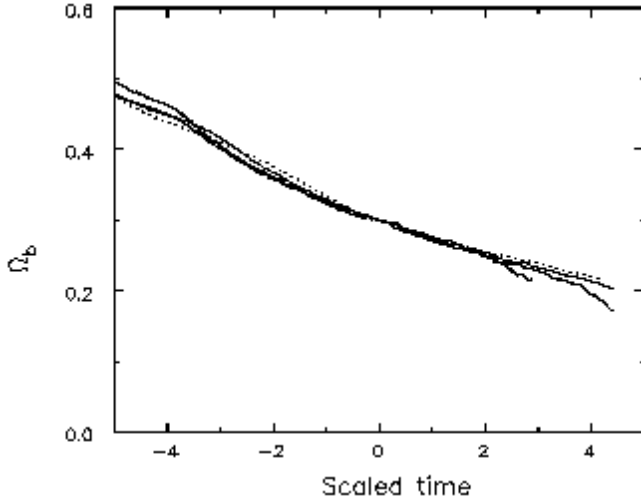


FIG. 5.— The bar pattern speed as a function of normalized time for a series of experiments with differing mass bars, but all other properties held fixed. Bar masses are 0.5%, 1%, & 2% (all solid lines) and 5% (dotted line) of the halo mass. The times are scaled by the bar masses and shifted horizontally to coincide when $\Omega_b = 0.3$.

Debattista & Sellwood (1998, 2000), to reproduce the frictional drag quite accurately. Thus the suggestion by Valenzuela & Klypin (2003) that their different result was due to inadequate spatial resolution in the earlier work is unlikely to be correct. The different results obtained in these two studies will be discussed further in Paper II.

4.4. Other halo density profiles

Figure 4(a) shows the variation of Θ with angular speed for the Plummer halo, while Fig. 4(b) is for the singular isothermal sphere (SIS). These are directly comparable with Fig. 2(a), which is for the Hernquist halo. The angular velocity dependence of the frictional acceleration is noticeably different in both cases.

The bar in the Plummer halo has a semi-major axis $a = R_p$ and a mass $M_b = 0.02M_h$. Friction has two approximately equal peaks when $\Omega_b \simeq 1.4$ and $\Omega_b \simeq 0.7$, but the angular speed of this bar must drop to $2^{-3/4} \simeq 0.6$ before corotation moves outside the bar.

The behavior for the SIS is different again. Corotation is at the end of the bar when $\Omega_b = 1$, where friction is again past its peak. Note that features can arise in this curve because the scale-free nature of this model is broken in two ways: the perturbation has a definite linear size and the energy range of the active particles is restricted. The mass of the bar in this case, $M_b = 0.2aV_0^2/G$.

These curves, and that in Fig. 2(a), indicate the functional form of Θ in eq. (3). Since the bar is the same in all three cases, the differences stem directly from differences in the halo mass profiles, which affect the frequencies and particle density at the different resonances. Such differences are the analog of having a different velocity distribution for the background particles in the Chandrasekhar problem.

5. SCALING WITH OTHER PARAMETERS

In this section, I check directly whether the acceleration scales with bar mass, halo density and halo velocity

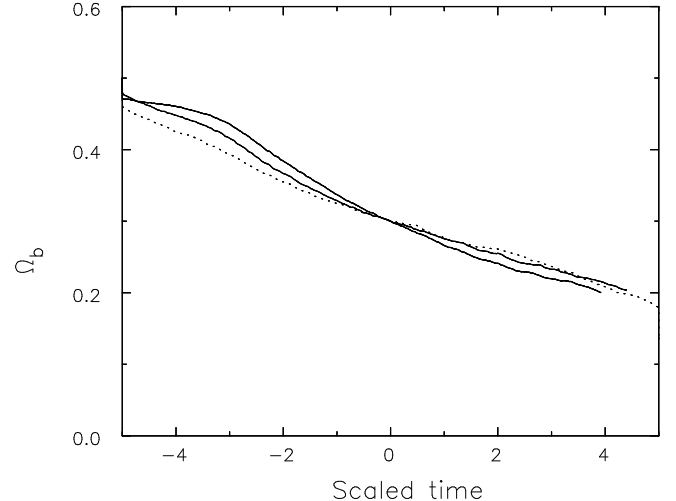


FIG. 6.— As for Fig. 5, but for the case when the halo density is scaled. The dotted curve is for the case when the halo density is doubled. See §5.2 for details.

dispersion, as suggested by eq. (3). All experiments reported in this section employ 10M particles, as were also used for those shown in Figs. 2, 3, & 4, but the initial bar pattern speed is set at the more conventional value such that corotation is at the end of the bar. I illustrate these tests for the Hernquist halo; the other halo models scale about as well, except for the test with velocity dispersion, as discussed in §5.3.

5.1. Scaling with bar mass

Figure 5 shows the time evolution of the pattern speed for bars of different masses, in the Hernquist halo; the bar pattern speed is a smoother function than its acceleration. Each line in this Figure is from a run with a different bar mass in the range $0.005 \leq M_b/M_h \leq 0.05$ and $\Omega_b = 0.5$ initially; the time axis is scaled by M_b , and the curves have all been shifted horizontally to coincide at the moment at which $\Omega_b = 0.3$. The curves overlay almost perfectly, indicating that frictional acceleration scales linearly with M_b in this regime, as expected from eq. (3).

5.2. Scaling with halo density

Equation (1) predicts that the acceleration is proportional to the density of the background. In the present more realistic case, the density of the background is a function of radius and it might seem that I would have to evaluate the LBK torque for a number of different halos to obtain a testable prediction. Fortunately, there is a much simpler way to test for the density dependence: I simply scale the density of the entire halo without changing the potential well in which the particles move. This ploy is equivalent to treating some fraction of the halo as rigid if the density is reduced but, since the density and potential of the halo need not be self-consistent in these restricted experiments, it is also possible to increase its density. I adopt this admittedly artificial strategy here simply to test for the expected linear scaling.

Figure 6 shows the results with a 2% mass bar, with Hernquist halos that have 0.5, 1 and 2 times the density given in eq. (4). Again the time axis scale is proportional

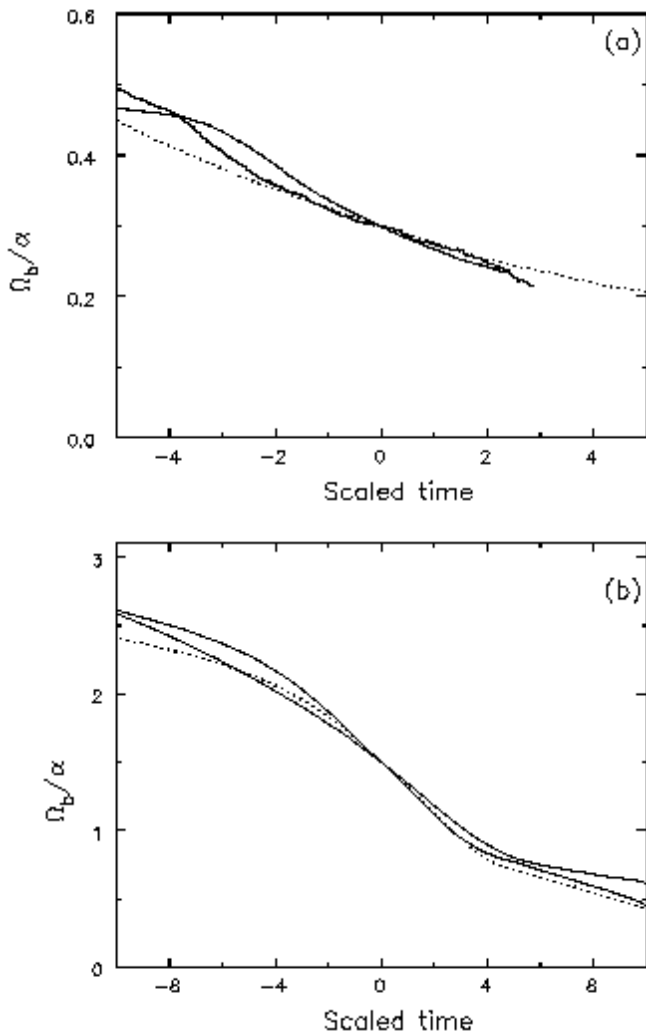


FIG. 7.— (a) As for Fig. 5, but for the case when the halo velocity dispersion and potential are scaled. The dotted curve is for the largest velocity dispersion. (b) Same as (a), but for the singular isothermal sphere. See §5.3 for details.

to the density, and curves are shifted so that they coincide when $\Omega_b = 0.3$. While not quite as convincing as Fig. 5, the similarity of the curves shows that the expected linear scaling holds approximately, in satisfactory agreement with the prediction of eq. (3).

5.3. Scaling with halo velocity dispersion

Finally, I test the scaling with velocity dispersion predicted by eq. (3). Again I employ a trick: by scaling the gravitational potential by a factor, α^2 , and the velocity dispersion, σ , by α , we continue to have an equilibrium model with an unchanged density profile. (The halo density and potential are no longer self-consistent, of course.) For this series of tests, however, I must also scale the bar pattern speed, since the argument of Θ contains the dispersion, σ .

Figure 7(a), which plots Ω_b/α as a function of $Mt\alpha^{-3}$, shows that when the velocity dispersion is increased or decreased by a factor $\sqrt{2}$, the evolution of the scaled bar angular speed does vary at approximately half or double the rate, respectively, as predicted by eq. (3), but the curves

do not match up as well as in Figs. 5 & 6.

Since scaling the potential well affects all the resonances, the particle density at each resonance does not scale in a simple manner, and formula (3) is too naïve. However, scaling should be restored in a scale-free model. The same scaling test with the SIS supports this expectation; the curves in Fig. 7(b) follow each other more closely than in Fig. 7(a), which was for the Hernquist halo.

5.4. Summary

The present problem differs from that considered by Chandrasekhar in many ways: the perturber is an extensive rigid body moving at changing angular frequency through an inhomogeneous sea of particles, which encounter the perturbation in a periodic fashion. Yet, this series of experiments has demonstrated that the deceleration of the bar caused by dynamical friction from non-interacting halo particles scales with bar mass and halo density as predicted by eq. (3), which so closely resembles Chandrasekhar's formula (1). The naïve scaling with velocity dispersion holds approximately for a general halo, and rather better for a self-similar halo, such as the SIS. The scaling with these parameters is an inevitable consequence of dynamical friction being second order effect caused by the interaction between the perturber and its own wake.

6. EXCHANGES AT RESONANCES

In this section, I present a more detailed analysis of one experiment in order to shed more light on resonant interactions, and the time-dependence of the frictional acceleration. The variation of $\Theta(\Omega_b)$ for this “fiducial” experiment is shown by the dotted line that starts with $\Omega_b = 0.5$ in Fig. 2(a) – *i.e.* the experiment with the lowest initial Ω_b , and the only one shown in this figure to start with corotation outside the bar.

6.1. Adiabatic invariants

The interaction between an orbit and a perturbing bar potential was discussed by Lynden-Bell (1979) in the analogous case of disks. In that geometry, the unperturbed orbit of a particle in resonance closes in the frame that rotates with the perturbation, and Lynden-Bell pointed out that a star close to a resonance could be regarded as pursuing a closed figure that precesses slowly relative to the major axis of the perturbation.

When $m = n$, for the disk-like resonances, the unperturbed orbit precesses at the rate $\Omega_{\mathbf{m}} \equiv (n\Omega_\phi + k\Omega_r)/m$. In general, $\Omega_{\mathbf{m}} \neq \Omega_b$, and the difference, $\Omega_{\mathbf{m}} - \Omega_b = \Omega_s$ is a slow frequency close to the resonance; *i.e.* $|\Omega_s/\Omega_\phi| \ll 1$. Since the time taken for the star to complete an orbit round the closed figure is short (one or two radial periods), the action $J_f \equiv J_r - kJ_\phi/m$, associated with this fast motion will be adiabatically invariant. On the other hand, the slow rate of precession of the orbit relative to the bar allows a large change to the “slow” action.

The situation is more complicated for the DRR, since the orbit does not close in the bar frame and the adiabatic invariant is the total angular momentum, L (WK05). Conservation of L might seemingly preclude any angular momentum exchanges with the bar. However, this resonance is most important for highly inclined orbits, and while L

is conserved, the plane of the orbit, and therefore L_z , is changed at the resonance; thus interactions at the DRR are able to slow the bar.

Because even quite mild potential perturbations can produce non-linear orbital responses at resonances in this manner, TW84 examined the resonant terms more carefully. They showed that second-order perturbation theory remains valid provided that particles make a “fast” passage through the resonance. By this, they mean that the pattern speed of the bar is changing sufficiently rapidly that “large non-linear resonant perturbations do not have time to develop before the star has crossed the resonance.” In effect, the star crosses the resonance in less than one libration period of the figure. Since the precession rate is slow, TW84 and Weinberg (1985) argued that fast passage through the resonance is the correct assumption, and second-order perturbation theory should be valid.

6.2. Individual orbits

Figure 8 presents a direct test of this assumption in the fiducial run. The time evolution of Ω_b is shown in panel (a), while panel (b) shows the evolution of the instantaneous L_z for ten particles orbiting in the mid-plane. The orbits shown are those of test particles run in a reconstruction of the time evolution of the total potential, which requires knowledge only of the bar phase at every step in the original simulation. All have the initial energy $E = -0.38$ and angular momentum, $L_z = 0.4L_{\max}(E)$ but are spaced equally in initial phases. The short-period oscillations in L_z of each particle are forced as each particle moves in the bar field. Larger, and lasting, changes occur as particles pass through a resonance. Individual orbits can either gain or lose, depending on their phase relative to the bar.

The group of particles selected is typical of the many hundreds I have examined. Large changes in L_z occur over the time interval $t \simeq 50$ to $t \simeq 200$ during which time Ω_b decreases from ~ 0.45 to ~ 0.4 . About half the particles gain in angular momentum by up to $\sim 20\%$ as they are caught in a corotation resonance, while the particles at other orbital phases lose similar amounts. These same particles also pass through an inner Lindblad resonance around $t \sim 1100$ where a majority gain L_z . Notice that friction is moderate when these particles pass through the CR, but that the late second blip in friction (Fig. 2a) occurs as the particles pass through the ILR. Many other in-plane orbits that I have examined also show two separate periods of angular momentum exchange with the bar.

It should be noted that the more tightly bound the orbit, the higher its intrinsic frequencies. Some of the most tightly bound orbits indeed pass through the ILR at early times, as stressed by WK05. However, these orbits are confined close to the center, where they couple weakly to the inner part of the perturbation, whose amplitude decays quadratically towards the center. Their consequent modest gains in angular momentum contribute little to the overall torque, which is dominated by the CR and OLR exchanges by larger orbits, as I show in §6.3. The bar has already become uninterestingly slow by the time the larger orbits cause strong friction at the ILR.

TW84 note that the frictional torque will be reduced, and the sign of the exchange between the particle and the perturbation difficult to predict, if the halo particles pass slowly through the resonance (as defined above). TW84

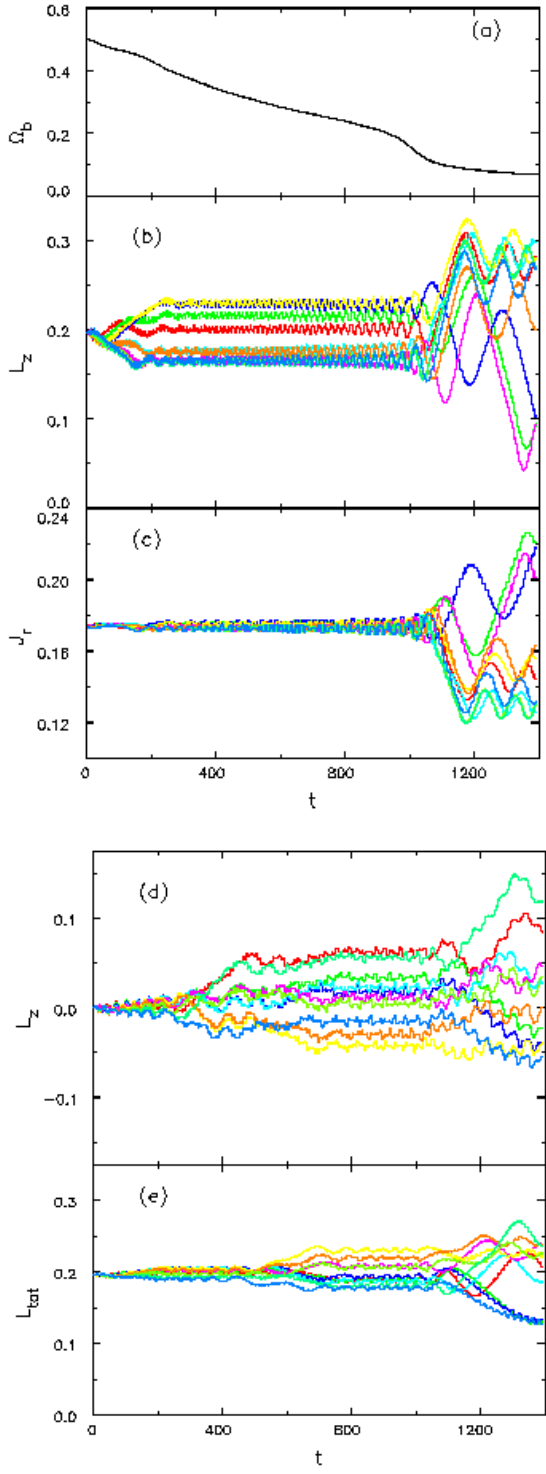


FIG. 8.— (a) The evolution of the pattern speed in the fiducial run. (b) The instantaneous angular momenta of ten particles as a function of time. The particles move in the mid-plane and all start with the same energy and angular momentum but have equally spaced phases. The quasi-periodic oscillations on each line are the forced response to the bar potential, the large changes, which are not modulated for the most part, are caused by passages through resonances. (c) An approximation to the radial action for the same orbits shown in (b). (d) The instantaneous z -component of angular momentum of a different ten particles that start on exactly polar orbits, but have the same energy and angular momentum as in (b) have equally spaced phases. (e) The total angular momentum of the particles shown in (d).

and Weinberg (1985) expected fast passage through the resonance, but offered no proof. Diagrams such as Figure 8(b) allow us to examine this key issue. The changes for each particle at CR are generally non-oscillatory, indicating that the particle is not librating in the resonance, and therefore the passage is fast. The story at the ILR is less clear, however, as the instantaneous L_z of each particle continues to oscillate right to the end. It is likely that these oscillations are simply the forced responses to the bar potential; their period seems to be about 100 time units, which is reasonable for precession of closed elliptical figures with respect to the slowly-rotating bar. These oscillations aside, the larger changes in L_z mostly, with perhaps a couple of exceptions, seem to occur within a single oscillation period.

Thus Figure 8(b), and hundreds of other orbits that I have examined, show that most passages through resonance can indeed be treated by the LBK approach. Since I have not examined every corner of phase space, this does not, of course, amount to a proof that the fast passage assumption is adequate, but it does suggest it is good for most orbits.

The adiabatic invariance of the fast action is also borne out, as shown in Fig. 8(c). Determination of the exact radial and azimuthal actions in a rotating and slowing, non-axisymmetric potential would be very difficult, but approximate values are good enough for our purpose here. The instantaneous value of $L_z \simeq J_\phi$, and we adopt $J_r \simeq 0.5a^2\pi/\tau$, where a is the semi-radial excursion of the particle and τ , the radial half-period, is determined by the time between the most recent passages through peri- and apo-center for the particle. (Properly-defined actions would not exhibit short-period oscillations, and the non-smooth variations of J_r at late times reflect a change in the estimated value each time the radial direction of the particle reverses.)

At the CR, $k = 0$ and therefore $J_f = J_r$; it can be seen that the approximate radial action is almost unchanged during the changes to L_z around $t \sim 100$. (Note the difference in scales between panels b and c.) The opposite is true for the changes around $t = 1100$, where it is clear that particles that gain L_z also lose J_r and *vice-versa*, as predicted by conservation of J_f when $k = -1$ for the ILR. In fact, $\Delta J_r \simeq -\Delta L_z/2$ in these cases, confirming that resonance responsible for these large changes is indeed the ILR.

Fig. 8(d) and (e) present a similar study of orbits that start with the same total angular momentum and energy as in (b) and (c), but which are initially oriented perpendicular to the bar plane so that $L_z = 0$ for all initially. These orbits pass through the DRR between $300 \lesssim t \lesssim 400$, and it can be seen that some gain L_z and others lose. However, panel (e) shows that the total L of these orbits does not change during this period, confirming that this resonance merely re-orient the plane of each orbit. (These same particles suffer changes to L at later times when they pass through other resonances.)

6.3. Integrated changes

It is interesting also to examine the changes to the distribution of particles about the main resonances as friction proceeds. Extracting this information from simulations is not completely straightforward because the an-

gular momentum of a resonant particle on a nearly circular orbit differs from that of another particle at the same resonance that has a highly eccentric orbit. Holley-Bockelmann, *et al.* (2003) and WK05 draw contours of the net changes of angular momentum over a short time interval in $(E, L/L_{\max})$ space, where $L_{\max}(E)$ is the specific angular momentum of a circular orbit of specific energy E . In order to suppress shot noise, these figures require considerable smoothing, even when very large numbers of particles are employed.

Perturbation theory (TW84, Weinberg 2004) indicates that friction depends on gradients of the DF w.r.t. both J_r and J_ϕ , although the coefficient of the radial action derivative is k , which is zero at CR. Since $J_f \equiv J_r - kJ_\phi/m$, is adiabatically invariant, changes in J_r must be related to changes to J_ϕ , and we need examine the distribution with respect to a single action only. The natural choice is L_z , the quantity of greatest interest for friction.

At any given resonance, the particles that undergo the largest changes have $\Omega_{\mathbf{m}} \simeq \Omega_b$. We define $f(J_r, J_\phi)$ to be the density of particles in the space of these two actions,² and determine the mean value of f at fixed $\Omega_{\mathbf{m}}$. The mean value is defined by the path integral

$$F(\Omega_{\mathbf{m}}) = \frac{\int_C f(J_r, J_\phi) dl}{\int_C dl}, \quad (10)$$

with the path C being the locus of constant $\Omega_{\mathbf{m}}$ through (J_r, J_ϕ) space from $J_r = 0$ to $J_\phi = 0$. In practice, the numerator is a kernel estimate from the values of $\Omega_{\mathbf{m}}$ computed from all the particles at each separate resonance. Since $\Omega_{\mathbf{m}}$ is a single-valued function of the angular momentum, L_{res} , of a circular orbit, I use this as the abscissa

$$F(L_{\text{res}}) = \frac{\sum_i w(L_{\text{res}} - L_{\text{res},i})}{\int_C dl}, \quad (11)$$

where $L_{\text{res},i}$ is the angular momentum of a circular orbit that has the same $\Omega_{\mathbf{m}}$ as the i -th particle, w is a kernel function, and the denominator is unchanged.

The average defined in eq. (10) is not a canonical transformation, and therefore does not preserve phase space volume. Thus we cannot expect the gradient of $F(L_{\text{res}})$ to be a completely reliable surrogate for the gradients in the DF – a Jacobian factor may alter the slope. But since F is defined as the average of f at fixed frequency difference from the resonance, we should expect its slope to give a general indication.

Figure 9 shows the function $F(L_{\text{res}})$ at the ILR, CR, OLR and DRR at two separate times during the evolution of the fiducial model. A significant fraction of the particles in the simulation, of order 10%, contributes to the curve in each panel implying a rather low-level of shot noise.

The strongest feature is for CR at $t = 200$ (middle panel of top row), where F shows a clear peak just to the low- L side of the resonance, which is marked by the vertical line. Near to the resonance, particles cross corotation in both directions on horse-shoe orbits (Binney & Tremaine 1987, §7.5) as they gain and lose L_z . The negative gradient in F implies there are more particles on the low- L side, and

²This is not the distribution function as usually defined, but is the DF integrated over all orbit phases and the inclination angle of the orbit plane θ .

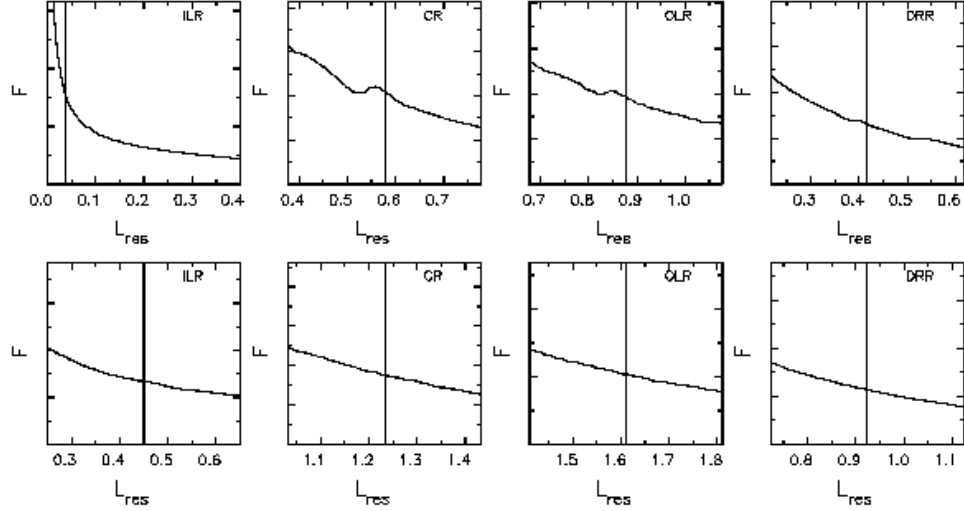


FIG. 9.— The function $F(L_{\text{res}})$ as defined in the text at the most important resonances at two different times in the fiducial simulation; the top row shows curves at $t = 200$, while the bottom row is for $t = 1000$. The vertical line shows location of the resonance at the moment illustrated, and the range of abscissae is set to show a region around the resonance containing $\sim 10\%$ of the halo particles. The vertical scale is linear from zero, but is otherwise arbitrary.

therefore an excess of gainers over losers. This imbalance causes a net gain of angular momentum by the particles, and therefore a net loss by the bar – producing the required friction.

If the pattern speed were to stay constant, the imbalance would tend to flatten the slope of F , and the distribution of particles about the resonance would approach kinetic equilibrium in which there would be more nearly equal numbers of particles crossing in both directions. But as Ω_p declines, the resonance keeps moving to larger L_{res} (frequency is decreasing function of angular momentum), and equilibrium is never established; instead, the density of particles about the dominant resonance(s) responsible for friction maintains a shoulder, or excess of particles, on the low- L side of the resonance, as shown in Fig. 9.

The pronounced feature at CR at $t = 200$ is characteristic of the distribution over most of the evolution, and changes at CR dominate the torque. A similar, but less pronounced, feature can be seen at the OLR at $t = 200$, but its importance fades as the bar slows. The DRR also shows a definite, though weaker, feature at $t = 200$; note that the range of L_{res} seemingly overlaps that shown in the panel labeled CR, yet $F(L_{\text{res}})$ is almost featureless near this value because the function is computed for a different resonance. The DRR feature persists for about the same duration as the CR, but is again too weak to be visible at the last time shown.

The dominance of CR also fades in the latest stages when the bar speed has more than halved. A very mild flattening of F at the ILR is possibly present at $t = 1000$, and is the only indication I could find in plots of $F(L_{\text{res}})$ of changes to $F(L_{\text{res}})$ at this resonance. However, the weakness of features in $F(L_{\text{res}})$ at this resonance does not imply that no changes occur; indeed Fig. 8 shows that substantial interactions are taking place at the ILR around this time. The weakness of this feature at the ILR may indicate that exchanges at this resonance are not self-reinforcing, in contrast to those at other major resonances. Alternatively, features may be suppressed by two effects: the most

important is that the instantaneous angular momenta of particles that have passed through the ILR oscillate by amplitudes of typically 0.05 (see Fig. 8c), which may be sufficient to wash out intrinsic features. Second, conservation of J_f at this resonance implies that changes in J_r must be reflected in changes of the opposite sign in L_z , leading to partial cancellation in the net change in L_z .

7. TIME DEPENDENCE

Weinberg (2004) finds that the LBK torque formula from TW84 does not predict the correct time evolution of the bar pattern speed; he was able to obtain approximate agreement with his experimental results only by taking the history of the bar perturbation into account. His formula for the torque in the time-dependent regime is also of the form eq. (3), but with a function Θ that now depends on the entire history of the perturbation.

Since a theoretical prediction invites comparison, I have tried experiments similar to that reported by Weinberg. The solid curve in Figure 10 shows the pattern speed evolution using my code with the bar and NFW halo (see Appendix) that Weinberg employed for his first test. The axes have been scaled to the units adopted by Weinberg and I have reproduced the curves from his figure (see also Fig. 16 of WK05); his time-dependent, linear theory prediction is shown by the dashed curve and Weinberg's own simulation is shown by the dot-dashed curve. Both curves differ from each other and from my result, although the differences are minor.

The small differences from both Weinberg's theoretical prediction and from his simulation do appear to be significant, however. I have checked that my result does not depend on any numerical parameters; increasing the number of particles to 10M, halving the time step, increasing the outer truncation radius by 50%, and other tests all yielded results that differ from the solid curve shown by scarcely more than the thickness of the line. I have also verified that total angular momentum is conserved to 0.3% of the small total possessed by the bar at the start.

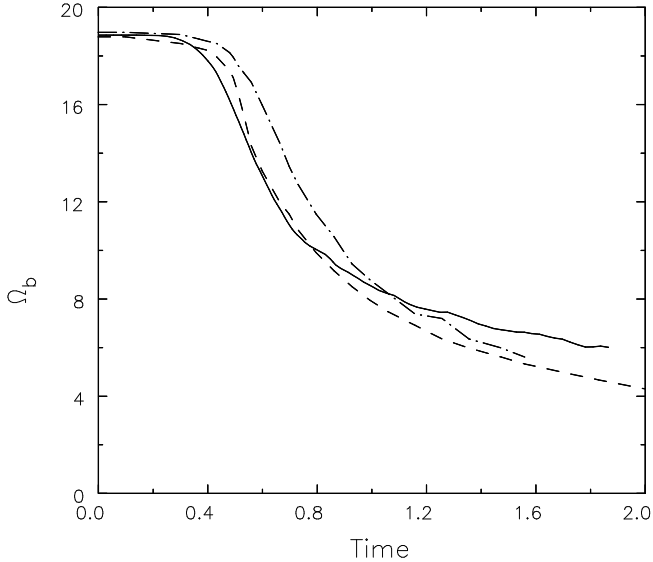


FIG. 10.— The dashed line reproduces Weinberg’s (2004) prediction from perturbation theory for the pattern speed evolution, while the dot-dash line shows his N -body simulation result; the model he used is described in the Appendix. The solid line shows the evolution in my experiment for the same case. See §7 for details.

Weinberg’s prediction requires sophisticated numerical treatment of a stiff system of coupled equations, and differences from my simulation could possibly result from numerical inadequacies in his prediction. It is harder to understand why Weinberg’s simulation differs from mine, as I have found my result to be so robust.

Returning to Fig. 2(a), the various dotted curves indicate a strong, and long-lasting, dependence on the initial pattern speed. I have examined orbits and F for the dramatically stronger friction exhibited by the curve shown by the solid line in this figure, in the same manner as for the fiducial model reported in §6. I find that the stronger drag at a given Ω_b when the pattern speed is started from a higher value arises from a steeper local gradient in $F(L_{\text{res}})$ because the shoulder is more pronounced than that shown in Fig. 9. The resonance lies in similar position relative to the peak, but the higher peak has steeper slopes. The shoulder is more pronounced because the higher starting speed enables more particles at higher frequencies to be caught in the CR, and to experience much larger changes in L_z (some gain by up to factors of 5).

7.1. Discussion of time-dependence

In hindsight, the importance of time-dependence is entirely reasonable. It is clear from the distribution of particles about the CR and OLR shown in Fig. 9 that the local slope of F depends on the past history of resonant interactions. As it develops, friction sculpts the DF in the vicinity of the dominant resonance, which in turn affects the strength of the subsequent frictional drag. Thus the limit of a steady bar rotating at fixed Ω_b , which was adopted by TW84, does not capture the true story; Weinberg’s (2004) re-derivation using Laplace transforms is essential.

The very strong dependence of the acceleration on the starting angular frequency reported in Fig. 2(a) is reflected

in the magnitude of the shoulder, and the local gradient in F at the resonance. The curves in that figure seem to converge for smaller values of Ω_b , suggesting somewhat less extreme dependence on past history in the physically more reasonable regime where corotation is beyond the end of the bar.

Figs. 5 – 7 show that the scaling of the frictional force with the main parameters of eq. (3) still holds, at least approximately, despite the complication of time-dependence, as Weinberg also notes. Note that the perturbation has the same initial Ω_b and turn-on rule for the bar mass and halo density tests, so that the time-dependence of the function Θ did not change. However, the initial bar pattern speed had to be scaled in the experiments with different velocity dispersion, making the reasonable agreement shown in Fig. 7(b) all the more reassuring.

8. CONVERGENCE TEST

As noted earlier, halo particles gain angular momentum, on average, at resonances. Even though each may pass through the resonance rapidly, we will not obtain the smooth torque expected in the continuum limit unless there are many particles, densely spread over a broad range of frequencies. The required number depends on the width of the resonance in frequency space: If the bar had a fixed or very slowly changing pattern speed, the resonances would be sharp and the simulations would indeed require a very large N (Weinberg & Katz 2002; Holley-Bockelmann, *et al.* 2003; WK05), but the forcing frequency is broadened by its decreasing angular speed and we can hope that the discreteness of the particle distribution will become insignificant for some attainable N .

Figure 11 shows that the pattern speed evolution in the Hernquist halo appears to converge to a smooth function as N increases. Merely 10^4 particles are sufficient to obtain qualitatively correct behavior for the 5% mass bar, but almost one hundred times larger N is needed for comparable numerical quality with a bar of one tenth this mass. Phase space needs to be populated more densely as the mass of the bar decreases, in order that a large enough number of particles are passing through the resonance at any time to yield a smoothly varying force. Both the effective potential of the resonance is weaker, and the Lorentzian frequency width of the resonance is reduced by the slower braking rate. As both factors vary with the mass of the perturber, it seems reasonable that the number of particles needed to obtain smoothly varying friction should increase faster than M_b^{-1} . However, one million is adequate even for a low-mass bar.

The smoothness of the braking rate in Figs. 2 & 4, and for large N in Fig. 11, is evidence that the resonant exchanges which give rise to the force are dense enough at most frequencies to produce a smooth torque. The frictional force may become erratic at very low pattern speed (Fig. 2a) because phase space is not populated densely enough as $|\dot{\Omega}_b|$ decreases, but this is a physically uninteresting regime.

These empirical results conflict with the recent claims by WK05 that a much larger number of particles is needed to obtain the correct result. However, their analysis does not take proper account of the changing pattern speed, which is so important. The time dependence of the frictional

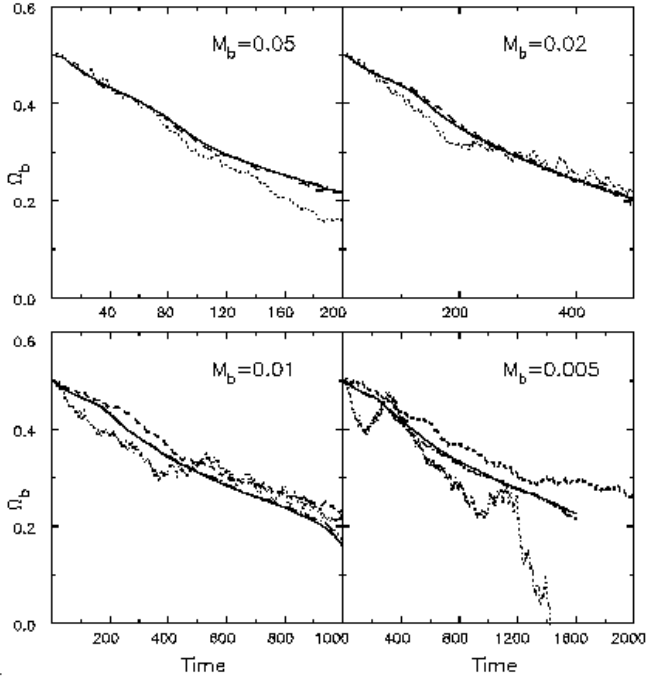


FIG. 11.— The bar pattern speed as a function of time for experiments with differing mass bars, each for four separate values of N . The indicated bar masses are fractions of M_h and the length of the time axis is inversely proportional to the bar mass in each panel. The line styles indicate the number of particles: $N = 10^4$ – dotted, $N = 10^5$ – dashed, $N = 10^6$ – dot-dashed, and $N = 10^7$ – solid.

force arises from preceding changes to the DF, and the shoulders in Fig. 9 indicate directly just how broad the resonance is. The feature can develop and behave as it does only if particles with angular momenta as far away as the width of the shoulder from the precise resonance are being affected by the resonance. Since $\sim 10\%$ of all halo particles contribute to each panel, it appears that $\gtrsim 1\%$ of all halo particles take part in exchanges at a dominant resonance at any moment. The convergence tests in Fig. 11 confirm that stochastic behavior when resonances are too sparsely populated (what WK05 describe as “coverage”) is brought under control at comparatively low- N , when the pattern speed changes at realistic rates.

It should be noted that these experiments reveal only the number of particles needed to populate phase space densely enough for the frictional force to approximate the continuum limit in the absence of self-gravity. The issue of collisional relaxation also needs to be addressed when the particles interact with each other, which may require more particles, as I discuss in §9.3.

9. EFFECT OF SELF-GRAVITY IN THE HALO

All experiments reported so far treat the halo as a non-interacting population of test particles, which move in a fixed potential well and respond only to the perturber, as in the usual treatment of dynamical friction (*e.g.* BT). Collective effects in a collisionless halo could also be important, however, because the wake itself contributes to the non-axisymmetric density affecting the orbits of the halo particles. Hernquist & Weinberg (1992), Weinberg & Katz (2002), and Sellwood (2003) have already reported

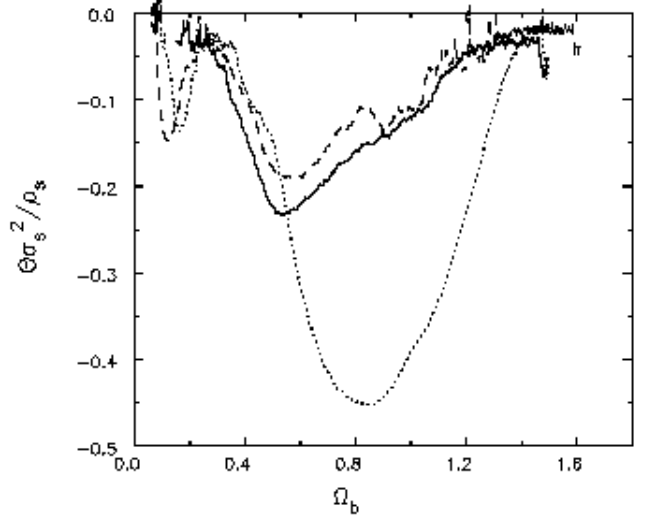


FIG. 12.— The acceleration of the bar when self-gravity of the halo response is included. The solid curve shows the behavior when all terms $0 \leq l \leq 4$ are included, the dashed curve shows the situation when only the $l = 2$ terms are employed. The dotted curve shows the corresponding case with no self-gravity, the fiducial model, reproduced from Fig. 2(a).

some experiments with rigid bars that take this into account, but the emphasis in those papers was on the change to the halo density profile.

Here I study the effect of self-gravity on the frictional force, while still employing an imposed bar. I break the discussion of collective effects into two levels of complication: when self-gravity includes the monopole terms, the radial mass profile of the halo could possibly change substantially over time, as claimed by Weinberg & Katz (2002). I therefore begin by including only the quadrupole field of the response density, before describing how other terms affect the evolution. Note that all the experiments described in this paper are perturbed with the non-axisymmetric field of a rigid bar. Fully self-consistent simulations, with the bar also made of responsive particles, are reported in other work (*e.g.* Papers II & III).

I compute the self-gravity of the halo using the method described by McGlynn (1984) and Sellwood (2003, Appendix A). Briefly I use a 1-D spherical grid, with an expansion of the gravitational field up to order l_{\max} in surface harmonics on each radial shell of the spherical grid.

9.1. Quadrupole field of the response

The dashed curve in Figure 12 shows the bar acceleration when only the quadrupole field of the halo response density is included; the dotted curve, reproduced from Fig. 2(a), shows the behavior with no self-gravity. It is clear that the self-gravity term increases the drag slightly when the pattern speed is slow, but greatly *diminishes* it when the bar has an artificially high pattern speed.

This behavior is a consequence of the phase of the halo response. Including the self-gravity of the response weakens the net torque on the bar when the response is more than 45° out of phase with the imposed bar; the phase lag when self-gravity is included is somewhat similar to that shown in Fig. 2(b), but the response remains more nearly perpendicular for longer. As the bar slows, the re-

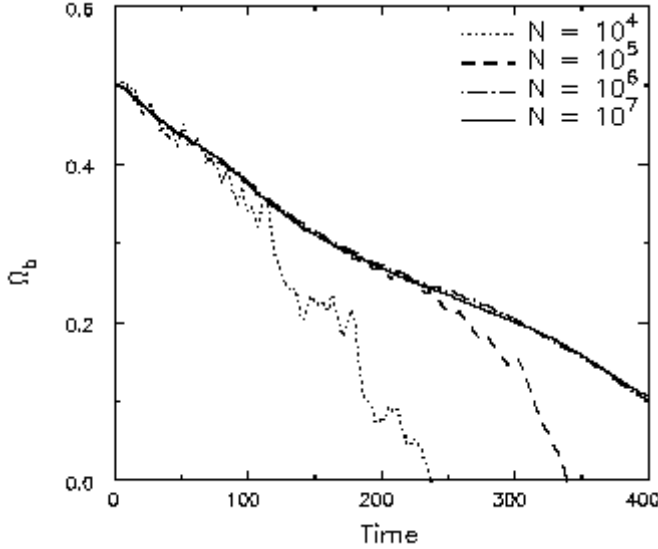


FIG. 13.— The evolution of the pattern speed of a 2% mass bar which starts with corotation at the end of the bar ($a = r_H$), for experiments with different N . Unlike for Fig. 11, these experiments include all low-order self-gravity terms of the halo particles ($l \leq 4$).

sponse gradually shifts towards alignment with the bar, thereby augmenting the quadrupole field of the perturbation and causing modestly increased friction. Note that friction peaks at $\Omega_b \simeq 0.5$ when corotation is at the end of the bar, implying that self-gravity always enhances friction in the physically relevant regime.

9.2. Including the monopole and other terms

The solid line in Fig. 12 shows the effect of adding more terms to the self-gravity of the halo response; in this case all $l \leq 4$ terms. The addition of these extra self-gravity terms increases friction somewhat at most angular speeds over that obtained when only $l = 2$ terms are used.

9.3. Convergence test

Figure 13 shows the effect of changing the particle number, N . I use the Hernquist halo, a bar with $M_b = 0.02M_h$, and a more realistic initial Ω_b . This test includes all $l \leq 4$ terms of the self-gravity of the halo density response and thus some collisional relaxation must be present.

As without self-gravity, the time variation of the pattern speed becomes smoother as N increases. The evolution is closely similar for the two cases with $N \geq 10^6$, but friction is clearly overestimated when $N = 10^4$ and slightly so when $N = 10^5$. The minimal differences between the results for the experiments with $N = 10^6$ and $N = 10^7$ indicate that 1M particles is a sufficient number to capture the correct physics for this case with a low-mass bar.

The 2% mass bar used in Fig. 13 is the same as for the second most strongly braked case in Fig. 11. Comparison of these two convergence tests indicates that the low- N models depart more strongly from the high- N results when self-gravity is included. However, the number of particles needed for convergence is not increased dramatically by self-gravity. Thus, Weinberg & Katz (2002) and Holley-Bockelmann, *et al.* (2003) are correct that the reduction in orbit quality caused by numerical noise in self-gravitating

halos does affect the friction force, but the torque converges for reasonably accessible numbers of particles; 1M appears to be plenty in this problem, as Sellwood (2003) concluded from fully self-consistent experiments.

Note also the complete absence of numerical noise in the higher- N experiments shown in Figs. 11 & 13. The convergence is truly impressive; curves for which N differs by factors of 10 overlay almost perfectly, and there is little evidence of differences due to shot noise.³ It seems inconceivable that such impressive convergence could be achieved if Weinberg's arguments (*e.g.* Weinberg & Katz 2002 and subsequent papers) for the much higher number of particles needed were correct.

In this vein, it should also be noted that my earlier work to reproduce the normal modes of disks (*e.g.* Sellwood 1983; Earn & Sellwood 1995) already demonstrated that simulations with modest numbers of particles could capture global instabilities, which are driven by resonant interactions between particles and rotating potential perturbations. The eigenfrequency predicted from linear theory can be reproduced to a precision of a percent or two in simulations with a few tens of thousands of particles. Admittedly these results were for a dynamical instability in a thin disk, whereas halo friction is a secular effect in 3-D. However razor-thin disks with random motion are scarcely more complicated than a spherical model, where each orbit is confined to its own plane. Furthermore, since the evolution in both cases is determined by the resonant terms, they have similar requirements for phase coverage of particles at the resonance, the ability of the resonance to persist for a large number of dynamical times, *etc.*, and there is no clear reason why particle number need be orders of magnitude higher for secular evolution than for instability.

9.4. Claimed counter-example

Holley-Bockelmann, *et al.* (2003) report fully self-consistent experiments for which the behavior with $N = 1\text{M}$ differs from similar experiments with larger N . However, the difference does not necessarily support their conclusion that 1M particles is inadequate for bar-halo interaction. They show (their Fig. 20) that the quadrupole field in the 1M particle experiment is weaker, so the halo torque *must* also be weaker, which implies that the lower halo particle number could still be adequate. Both Weinberg & Katz (2002) and Sellwood (2003) report that smaller N leads to more rapid angular momentum transfer, as also shown in Fig. 13, making the inadequate- N interpretation in this case still less plausible. Holley-Bockelmann, *et al.* do indeed have a result that is N -dependent, but the effect of lower particle number is to decrease the strength of the $m = 2$ distortion in the disk, and is therefore a consequence of disk dynamics and not halo friction. It is likely that a higher noise level in their lower- N disk interferes with their bar triggering mechanism. Specifically, they start with a bar-unstable disk and also apply a transient tidal field to trigger the bar; the smaller the number of particles, the larger the initial amplitude of the intrinsic

³This aspect is, in part, due to the careful selection of particles from the DF for the initial set-up (see Debattista & Sellwood 2000 Appendix B); random selection of particles inevitably leaves \sqrt{N} -type variations in the density of particles as a function of the integrals and does not, therefore, achieve quite such impressive convergence.

instability, which will generally interfere with the applied tidal field leading to a weaker bar, unless the phases of the two bar-forming mechanisms happened to be nearly aligned.

10. CONCLUSIONS

I have shown that dynamical friction between a rotating, imposed bar and a halo scales in a very similar manner to that predicted by Chandrasekhar's formula. The experiments reported in §§4 & 5 are highly idealized and employed the simplest possible system that could capture dynamical friction on a bar rotating in a halo. The retarding acceleration depends on the angular speed of the bar, scales linearly with its mass (*i.e.* the strength of its quadrupole field) and with the background density. It also scales roughly inversely as the square of the velocity dispersion of the background through which it moves, although this scaling is more approximate unless the model is self-similar. This result is the analog for a bar of that obtained by Lin & Tremaine (1983) from a similar study with orbiting satellites.

Even though the physical situation is quite different from rectilinear motion through an infinite, uniform background, and complicated by the existence of resonances and bar turn-on issues, the Chandrasekhar scaling still holds. It holds, because dynamical friction is fundamentally a second order effect that arises from the interaction of a perturber with its own wake. The strength of the interaction does depend on the details, but the parameter scaling cannot.

In all three halo types employed here, friction is weak when the bar pattern speed is so high that corotation is well inside the bar. As the bar slows, the frictional drag grows at first but generally peaks before corotation reaches the bar end. Thus, in the physically interesting regime, where corotation is beyond the end of the bar, friction always decreases as the bar slows in these non-rotating halos.

Friction is dominated by the quadrupole field of the bar both because the quadrupole is the dominant potential component of the bar, but also because the higher-order resonances that are associated with the higher expansion terms couple less strongly to the particles. Since the lowest-order, non-axisymmetric component of the bar field dominates, friction can be captured adequately in simulations with even quite low spatial resolution, provided enough particles are employed.

Tremaine & Weinberg (1984) first demonstrated that friction arises as the perturbation sweeps across resonances with the particles, a point stressed in recent work by Weinberg and his co-workers and by Athanassoula (2003). I have shown that the pattern speed of the bar changes sufficiently rapidly that a halo particle generally passes through the resonance without any complicated non-linear trapping, as expected by TW84. The forced responses of the halo particles change from anti-alignment to alignment with the bar as the pattern speed crosses a resonance, which happens smoothly because the resonance is broadened by the changing pattern speed. The net effect is to produce a global density response that lags the bar, causing the frictional drag. The lag angle between the bar and the halo response varies with the friction force, as shown in Fig. 2(b); it is close to 45° when friction is strong, but

the halo response is closely aligned with the bar when the bar is slow, and almost orthogonal when the bar is unreasonably fast.

Since one of the two actions associated with the unperturbed motion is adiabatically invariant, exchanges at resonances can be examined as a function of a single angular momentum-like variable, which I denote L_{res} . The density of particles is generally a decreasing function L_{res} , although previous angular momentum exchanges with the bar cause a local shoulder to develop at the most important resonances. The distribution with L_{res} evolves most strongly at corotation at physically interesting pattern speeds, but smaller changes are detectable at other resonances before the bar has slowed much.

The sculpturing of the particle distribution about the principal resonances by previous friction seems to be the reason for the strong dependence of friction on the previous evolution, discovered by Weinberg (2004). The magnitude of the friction force is determined by the local gradient in F , which differs from that in the initial model because previous exchanges with the perturbation have rearranged the particle distribution. A possibly similar effect may happen in proto-planetary disks (Artymowicz 2004), although self-reinforcing responses in that context have been found only at corotation, whereas I have found them at other resonances also.

In the absence of self-gravity, the number of particles needed to obtain a smoothly varying frictional force is quite modest, unless the bar is very weak. The main requirement here is that the broadened resonances caused by the time-varying pattern speed should overlap many particles in order to obtain the correct density response. The pattern speed changes more slowly for weaker bars, decreasing the frequency width of the perturbation and consequently raising the particle number needed to obtain a smoothly varying force. The number of particles needed in this regime appears to rise more steeply than the inverse of the quadrupole field strength.

Weinberg & Katz (2002) and WK05 argue that collisional relaxation in simulations with self-gravity should increase the number of particles required to approach the continuum limit, because potential fluctuations arising from Poisson noise affect the orbital behavior. The lowest-energy orbits, which they find are most delicate, should make a negligible contribution to the torque. I have found a small reduction in force quality when self-gravity is included, consistent with the prediction by these authors, but quite modest particle numbers are needed to bring this problem under control. Thus the frictional torque can be simulated accurately with standard algorithms and readily accessible computers.

All experiments reported here employ an imposed bar potential in order to examine the dependence of the halo response on the bar parameters. This simplifying approximation has many obvious disadvantages, as noted in §3. Fully self-consistent simulations, such as those to be reported in later papers in this series, are the only way to ensure that the bar forms with a dynamically realistic amplitude and pattern speed and responds to friction in the appropriate way.

I am grateful to Martin Weinberg for very helpful discussions, running some tests for comparison, sending a draft

of his preprint, and for comments on an earlier draft of this paper. I also thank Victor Debattista for many thoughtful suggestions, Kelly Holley-Bockelmann, Tad Pryor, and Juntai Shen for input, and Scott Tremaine for some helpful comments. An anonymous referee drew my attention to Artymowicz's paper. This work was begun while the author was a visiting member of the Institute for Advanced Study in Princeton; their hospitality is gratefully acknowledged. Grants from NASA (NAG 5-10110) and from NSF (AST-0098282) provided support.

REFERENCES

Arfken, G. 1985, *Mathematical Methods for Physicists*, 3rd ed. (Orlando: Academic Press)

Artymowicz, P. 2004, in *Debris Disks and the Formation of Planets: A Symposium in Memory of Fred Gillet*, ed. L. Caroff, L. J. Moon, D. Blackman & E. Praton (ASP Conf series 324), p. 39

Athanassoula, E. 1996, in *Barred Galaxies*, IAU Colloq. **157**, ed. R. Buta, D. A. Crocker & B. G. Elmegreen (ASP Conf series 91), p. 309

Athanassoula, E. 2003, MNRAS, **341**, 1179

Binney, J. & Tremaine, S. 1987, *Galactic Dynamics* (Princeton: Princeton University Press) (BT)

Chandrasekhar, S. 1943, ApJ, **97**, 255

Debattista, V. P. & Sellwood, J. A. 1998, ApJ, **493**, L5

Debattista, V. P. & Sellwood, J. A. 2000, ApJ, **543**, 704

Hernquist, L. 1990, ApJ, **356**, 359

Hernquist, L. & Weinberg, M. D. 1992, ApJ, **400**, 80

Holley-Bockelmann, K. & Weinberg, M. 2005, DDA abstract 36.0512

Holley-Bockelmann, K., Weinberg, M. & Katz, N. 2003, astro-ph/0306374

Kalnajs, A. J. 1977, ApJ, **212**, 637

Lin, D. N. C. & Tremaine, S. 1983, ApJ, **264**, 364

Little, B. & Carlberg, R. G. 1991, MNRAS, **250**, 161

Lynden-Bell, D. 1979, MNRAS, **187**, 101

Lynden-Bell, D. & Kalnajs, A. J. 1972, MNRAS, **157**, 1

McGlynn, T. A. 1984, ApJ, **281**, 13

Mulder, W. A. 1983, A&A, **117**, 9

Navarro, J. F., Frenk, C. S. & White, S. D. M. 1997, ApJ, **490**, 493

O'Neill, J. K. & Dubinski, J. 2003, MNRAS, **346**, 251

Sellwood, J. A. 1980, A&A, **89**, 296

Sellwood, J. A. 2003, ApJ, **587**, 638

Sellwood, J. A. & Debattista, V. P. 2005a, ApJ, submitted (Paper II)

Sellwood, J. A. & Debattista, V. P. 2005b, in preparation (Paper III)

Sellwood, J. A. & Debattista, V. P. 2005c, astro-ph/0508036

Tremaine, S. & Weinberg, M. D. 1984, MNRAS, **209**, 729 (TW84)

Valenzuela, O. & Klypin, A. 2003, MNRAS, **345**, 406

Weinberg, M. D. 1985, MNRAS, **213**, 451

Weinberg, M. D. 2004, astro-ph/0404169

Weinberg, M. D. & Katz, N. 2002, ApJ, **580**, 627

Weinberg, M. D. & Katz, N. 2005, astro-ph/0508166 (WK05)

APPENDIX

The NFW (Navarro, Frenk & White 1997) halo density profile is

$$\rho_{\text{NFW}} = \frac{\rho_s r_s^3}{r(r + r_s)^2}, \quad (1)$$

where ρ_s is a scale density and r_s is a scale length. The concentration parameter c is defined as the ratio of the “virial radius” to r_s ; at the virial radius, the *average* enclosed density is $200\rho_{\text{crit}} = 200 \times 3H_0^2/(8\pi G)$, with H_0 being Hubble's constant. Eddington's formula (Binney & Tremaine 1987, eq. 4-140b) yields an isotropic distribution function that is positive everywhere, but which requires some care to evaluate for the most bound energies.

Note that the NFW profile has a more slowly declining outer density gradient than does the Hernquist profile (eq. 4), but is otherwise closely similar. The density and

potential when $r < r_s$ are almost the same, while the logarithmic mass divergence of NFW profiles is both numerically inconvenient and physically unimportant – the extra mass at large radii has such low orbital frequencies and feels such a weak perturbing field from the distant quadrupole that its contribution to the total torque is negligible at pattern speeds of interest.

Weinberg (2004) uses an NFW halo with $c = 15$ for his first application of his formulae. I adopt his units for this case to facilitate comparison with his result; he chooses $15r_s$ to be his length unit, the mass interior to this radius as his mass unit, and he also sets Newton's constant $G = 1$. He chose a large, strong, heavy bar, with semi-major axis equal to $r_s = 1/15$, axis ratios $a : b : c = 1 : 0.2 : 0.05$, and a mass equal to half the halo mass interior to this radius, or 0.0526 of the virial mass. The initial pattern speed of the bar is 18.84 in his units, which places corotation at the bar end. The bar amplitude varies as $f(t) = [1 + \text{erf}(4t - 2)]/2$, where t is the time in Gyr for a halo scaled to the Milky Way; when $r_s = 20$ kpc, Weinberg's time unit is ~ 1.4 Gyr.